Inorganic Chemistry

ARTICLE

pubs.acs.org/IC

Characterization of Divalent and Trivalent Species Generated in the Chemical and Electrochemical Oxidation of a Dimeric Pincer Complex of Nickel

Denis M. Spasyuk,[†] Serge I. Gorelsky,[‡] Art van der Est,[§] and Davit Zargarian*[,†]

[†]Département de Chimie, Université de Montréal, Montréal, Québec H3C 3J7, Canada

[‡]Centre for Catalysis Research and Innovation and Department of Chemistry, University of Ottawa, Ottawa, Ontario K1N 6N5, Canada

[§]Department of Chemistry, Brock University, St. Catharines, Ontario L2S 3A1, Canada

Supporting Information

ABSTRACT: The electrolytic and chemical oxidation of the dimeric pincer complex $[\kappa^P,\kappa^C,\kappa^N,\mu^N$-(2,6-(*i*-$Pr_2POC_6H_3$-$CH_2NBn)Ni]_2$ (**1**; Bn = CH_2Ph) has been investigated by various analytic techniques. Cyclic voltammetry measurements have shown that **1** undergoes a quasi-reversible, one electron, Ni-based redox process ($\Delta E^0_{1/2}$ = −0.07 V vs $Cp_2Fe/[Cp_2Fe]^+$), and spectroelectrochemical measurements conducted on the product of the electrolytic oxidation, $[\mathbf{1}]^{+\bullet}$, have shown multiple low-energy electronic transitions in the range of 10000−15000 cm^{-1}. Computational studies using Density Functional Theory (B3LYP) have corroborated the experimentally obtained structure of **1**, provided the electronic structure description, and helped interpret the experimentally obtained absorption spectra for **1** and $[\mathbf{1}]^{+\cdot}$. These calculations indicate that the radical cation $[\mathbf{1}]^{+\cdot}$ is a dimeric, mixed-valent species (class III) wherein most of the spin density is delocalized over the two nickel centers ($Ni^{+2.5}{}_2N_2$), but some spin density is also present over the two nitrogen atoms ($Ni^{2+}{}_2N_2{}^{\cdot}$). Examination of alternative structures for open shell species generated from **1** has shown that the spin density distribution is highly sensitive toward changes in the ligand environment of the Ni ions. NMR, UV−vis, electron paramagnetic resonance (EPR), and single crystal X-ray diffraction analyses have shown that chemical oxidation of **1** with *N*-Bromosuccinimide (NBS) follows a complex process that gives multiple products, including the monomeric trivalent species $\kappa^P,\kappa^C,\kappa^N$-{2,6-(*i*-$Pr_2PO)(C_6H_3)(CH{=}NBn)$}$NiBr_2$ (**2**). These studies also indicate that oxidation of **1** with 1 equiv of NBS gives an unstable, paramagnetic intermediate that decomposes to a number of divalent species, including succinimide and the monomeric divalent complexes $\kappa^P,\kappa^C,\kappa^N$-{2,6-(*i*-$Pr_2PO)(C_6H_3)(CH{=}NBn)$}NiBr (**3**) and $\kappa^P,\kappa^C,\kappa^N$-{2,6-(*i*-$Pr_2PO)(C_6H_3)(CH_2N(H)Bn)$}$NiBr_2$ (**4**); a second equivalent of NBS then oxidizes **3** and **4** to **2** and other unidentified products. The divalent complex **3** was synthesized independently and shown to react with NBS or bromine to form its trivalent homologue **2**. The new complexes **2** and **3** have been characterized fully.

INTRODUCTION

Pincer complexes[1] have attracted much attention over the past two decades due, primarily, to their demonstrated potential in catalysis and materials science,[2] and the burgeoning interest in the chemistry of pincer complexes has led to a significant expansion in the type of pincer systems being investigated. Despite this expanding diversity, however, the vast majority of pincer complexes reported to date are monometallic species; moreover, a majority of the multimetallic pincer complexes reported to date feature "spacer-type" ligands as opposed to short bridging ligands (e.g., μ-halide, μ-OR, μ-NR_2, etc.) that might facilitate interactions between proximate metal centers.[3] Given the important role played by multimetallic complexes in probing paradigms such as cooperative reactivity and various intermetallic electronic interactions (e.g., electron transfer, magnetism, etc.),[4] multimetallic complexes based on pincer-type ligands should present interesting case studies.

During the course of our studies on pincer complexes of nickel,[5] we have synthesized the bimetallic species $[\kappa^P,\kappa^C,\kappa^N,\mu^N$-(2,6-(*i*-$Pr_2POC_6H_3CH_2NBn)Ni]_2$ (**1**; Bn = CH_2Ph) featuring two Ni^{II} centers bridged by the amide moiety of a new POCN-type pincer ligand (Chart 1).[5j] Noteworthy structural features of **1** include a puckered, cyclobutane-like Ni_2N_2 core and a *syn* orientation of the *N*-substituents; this compound is also an active catalyst for the Michael addition of ROH to acrylonitrile, which gives anti-Markovnikov products of alcoholysis. Complex **1** is a rare example of LXX pincer-type dinickel species,[6] but a

Received: December 30, 2010
Published: February 15, 2011

Chart 1

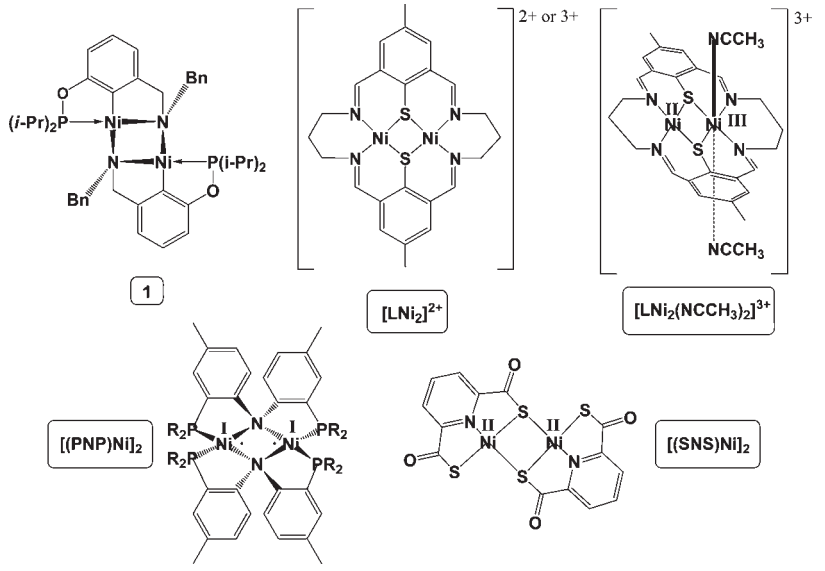

number of structurally related "pincer-like" dinickel complexes are known, including the complexes $[LNi^{II}_2]^{2+/3+}$,[7] $[LNi^{II}Ni^{III}(NCCH_3)_2]^{3+}$,[8] $[(SNS)Ni^{II}]_2$,[9] and $[(PNP)Ni^{I}]_2$[10] depicted in Chart 1. The latter species is a diradical featuring weak Ni−Ni interactions, whereas the other systems do not appear to involve any intermetallic interaction. Moreover, electron paramagnetic resonance (EPR) measurements and density functional theory (DFT) calculations have indicated that the spin density is localized mostly on *one* Ni center in $[LNi_2]^{3+}$ (ca. 70%)[7b] and $[LNi^{II}Ni^{III}(NCCH_3)_2]^{3+}$ (ca. 90% on the six coordinate Ni).[7b] These observations are thought to be relevant for understanding the reactivities of the active site in [NiFe] hydrogenases, for which these complexes are proposed as model systems.

Our interest in the chemistry of Ni^{III} pincer complexes[5e−5i] and the relatively facile access to **1** prompted us to examine the redox behavior of this dimeric species to answer some of the following questions: Would the dimeric structure of **1** be preserved upon oxidation? If so, would oxidation take place at both halves of the dimer or just one? In either case, how would the spin density be distributed over the Ni centers and the ligands? The generation of adjacent trivalent centers (or proximate ligand-based radicals) would be expected to give rise to varying degrees of spin-coupling and interesting magnetic properties, while single electron oxidation at nickel would generate a mixed-valent species of localized or delocalized spin density. A combination of spectroscopic, computational, and X-ray diffraction studies were undertaken to study the electrochemical and chemical oxidation of **1**, as reported herein.

RESULTS AND DISCUSSIONS

Electrochemical Oxidation of 1. Cyclic voltammetry measurements of **1** revealed a redox profile (Figure 1) that is qualitatively similar to those of its monomeric analogues (POCN)NiBr studied previously[5i] (POCN = 2,6-*i*-$Pr_2POC_6H_3CH_2NR_2$). This result implies that the observed oxidation

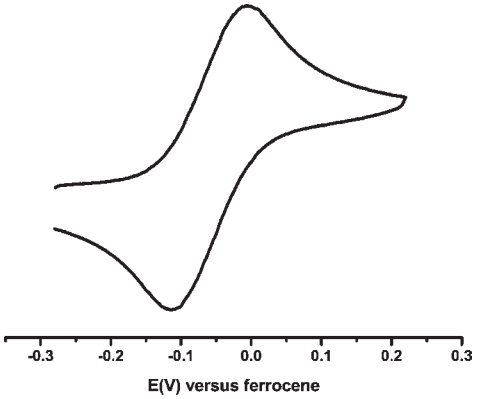

Figure 1. Cyclic voltammogram measured at 25 °C for a 1 mM dichloromethane solution of **1** containing tetrabutylammonium hexafluorophosphate as supporting electrolyte (0.1 M). The measurements were conducted using a glassy carbon working electrode at a scan rate of 100 mV/s. See Experimental Section for full details on the electrochemical studies.

of **1** is a quasi-reversible, Ni-based, one-electron process,[11] which rules out the possibility that electrochemical oxidation of **1** generates a doubly oxidized Ni^{III}/Ni^{III} species or leads to major structural reorganization that might entail collapse of the dimeric structure. The half cell potential $E^0_{1/2}$ of **1** (−0.07 V)[12] is much smaller than that of the monomeric amino analogues (POCN)NiBr (ca. +0.60 V[12] for NR_2 = NMe_2, NEt_2, and *N*-morpholinyl)[5i] and the above-cited dinickel species $[LNi_2]^{2+}$ (ca. +0.55 V[12]).[7] The facile oxidation of **1** can be attributed to the strongly electron-donating character of the amido moieties as well as the destabilizing (albeit weak) Ni−Ni interactions that would be expected to raise the energy of its highest occupied molecular orbital (HOMO, vide infra).

A spectroelectrochemical investigation of **1** was undertaken in an effort to detect the product(s) of its electrochemical oxidation

dx.doi.org/10.1021/ic1025894 |*Inorg. Chem.* 2011, 50, 2661–2674

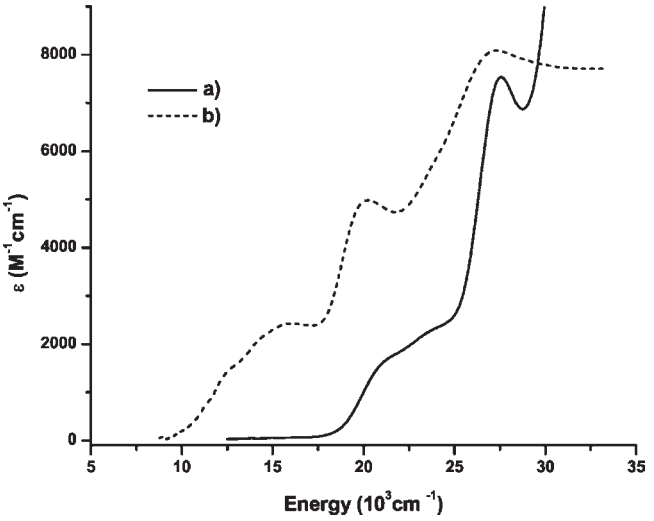

Figure 2. Absorption spectra of **1** in dichloromethane before (a) and after (b) the electrochemical oxidation at E_{ox} = 550 mV.

(eq 1). The electrolysis was carried out at 25 °C and 550 mV over 12 min on a 4 mM dichloromethane (DCM) solution of **1** containing $(n\text{-Bu})_4NPF_6$ as supporting electrolyte (0.1 M), and observed changes in absorbance were monitored by UV−vis−NIR spectroscopy (Figure 2). A gradual darkening of the sample was observed and an intensely dark solution was obtained at the end of the electrolysis. Consistent with the observed color of the solution, the absorption spectrum (Figure 2b) displayed multiple low-energy transitions in the range of 10000−15000 cm^{-1}; by comparison, the dinickel species $[LNi_2]^{3+}$ (Chart 1) exhibits a low-intensity absorption band at about 11000 cm^{-1} (ε = 85 M^{-1} cm^{-1}),[7b] whereas the absorption spectra of monomeric complexes (POCN)$Ni^{III}Br_2$ contain only bands higher than 15000 cm^{-1}.[5i] These differences in the absorption spectra imply important structural differences between $[\mathbf{1}]^{+\cdot}$ and (POCN)-$Ni^{III}Br_2$, suggesting that the dimeric structure of **1** survives its electrolytic oxidation. As will be discussed later, computational studies support this assertion and show that electronic transitions from occupied orbitals to the low-lying β-spin LUMO of $[\mathbf{1}]^{+\cdot}$ give rise to multiple bands in the near-IR and visible region of its absorption spectrum (vide infra).

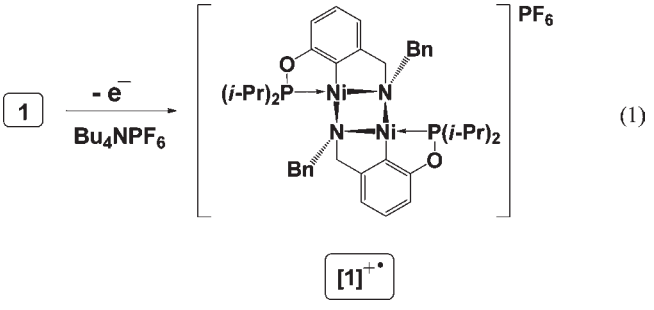

(1)

Chemical Oxidation of 1. The relatively low oxidation potential of **1** and the reversible nature of its redox process encouraged us to attempt a chemical oxidation and isolate the resulting species. Since previous studies had shown that *N*-Bromosuccinimide (NBS) and bromine are suitable oxidants for converting (POCN)NiBr to trivalent species,[5i] we investigated the reaction of **1** with these oxidants. Portion-wise addition of solid NBS to a concentrated solution of **1** in DCM caused an instantaneous darkening of the initially orange solution, and a brown mixture was formed when 2 equiv of NBS had been added; additional NBS resulted in the formation of an increasingly darker reaction mixture. Adding cold hexane to the nearly black reaction mixture containing **1** and 4 equiv of NBS resulted in the precipitation of an off-white solid, which was isolated by filtration and identified as succinimide. Storage of the dark filtrate at −18 °C for about one week gave a small crop of purplish-black crystals (23%) that were identified as the monomeric Ni^{III} species **2** featuring a new, imine-type POCN ligand (eq 2). The oxidation with bromine also produced **2**, but this reaction was less clean, producing a mixture of **2** and a greenish solid that we have not been able to identify.

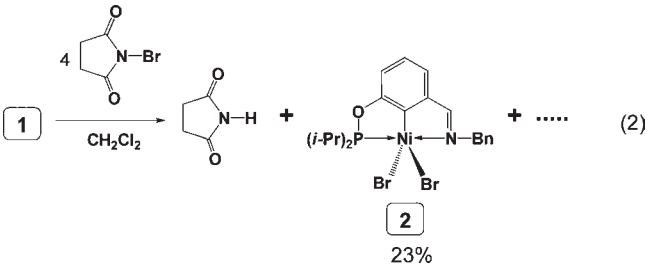

(2)

The observed formation of **2** involves oxidation of **1** at both the ligand ($ArCH_2NR \rightarrow ArCH{=}NR$) and the metal ($Ni^{II} \rightarrow Ni^{III}$),[13] which raises many questions about how and in what order the individual oxidation steps occur, and whether the entire process proceeds via a cascade-type mechanism or a stepwise path passing through observable intermediates. A number of studies have been carried out to answer these questions, beginning with the demonstration that the trivalent imine-type species **2** can be generated by oxidation of its divalent analogue **3**, which was prepared independently as illustrated in Scheme 1. Thus, the requisite imine-type POCN ligand was prepared in two high-yield steps: reaction of benzylamine with 3-hydroxybenzaldehyde gave the corresponding Schiff base (nearly quantitatively), which was then reacted with $(i\text{-Pr})_2PCl$ in the presence of base to give ligand **a** as a colorless oil (96%). Reaction of this new ligand with $NiBr_2(CH_3CN)_x$ and NEt_3 gave the corresponding pincer complex **3** in 89% yield, while treatment of the latter with 1 equiv of NBS in DCM gave the anticipated oxidation product **2** in about 62% yield; the oxidation gave a much better yield (94%) when 0.6 equiv of Br_2 was used as oxidant. These results demonstrate that the trivalent dibromo species **2** can, in principle, arise from its divalent monobromo analogue **3**. To determine whether **3** is indeed generated during the oxidation of **1**, we have examined the reaction of **1** with NBS using NMR, EPR, and UV−vis spectroscopy, as described below.

Monitoring Oxidation of 1 by NMR Spectroscopy. A 0.022 M DCM solution of **1** containing $O{=}PPh_3$ as internal standard was titrated with a 0.032 M solution of NBS, and the progress of the oxidation reaction was monitored by the changes in the color of the sample and its NMR signals. Thus, an instantaneous darkening of the solution was observed at the point of contact each time an aliquot of NBS was added. The deep brown spot dispersed after 2−3 s, but the initial yellow-orange color of the sample darkened gradually to a reddish-brown up to the addition of about 1 equiv of NBS; adding more NBS caused further

dx.doi.org/10.1021/ic1025894 |*Inorg. Chem.* 2011, 50, 2661–2674

Scheme 1

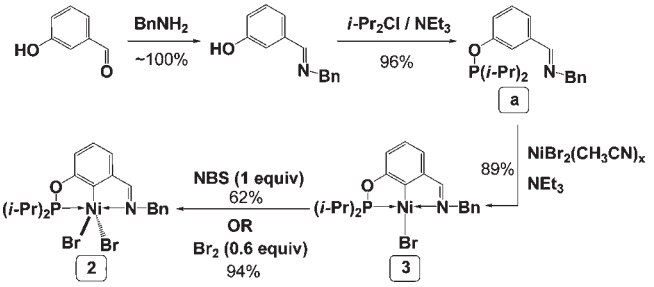

darkening of the sample, giving a deep-brown/black mixture at the end of the titration.

The $^{31}P\{^{1}H\}$ NMR spectrum of the sample containing the first 100 μL aliquot of NBS showed the emergence of a few new peaks in the chemical shift region of about 198−202 ppm, whereas subsequent additions of three more aliquots led to increases in the intensities of some of these signals and a commensurate decrease in the intensity of the precursor signal (at δ 193.16 in DCM). Addition of the fifth aliquot (ca. 1.2 equiv of NBS in total) caused a complete disappearance of the signal due to the starting material **1**, while additional aliquots of the oxidant led to a continuous decline in the signal intensities for all product peaks in comparison to the internal standard ($O{=}PPh_3$). Finally, addition of the 9-th aliquot (ca. 2.2 equiv of NBS in total) led to a complete disappearance of all ^{31}P signals.

The above observations indicate that the chemical oxidation of **1** proceeds in two distinct stages. The first, which takes place when less than 1 equiv of NBS is present in the mixture, involves the initial conversion of **1** to an intensely colored, short-lived species for which no spectral signature could be obtained; this species decomposes rapidly to give a few stable and diamagnetic species characterized by the appearance of a less intense color and the emergence of new and persistent ^{31}P signals. Close inspection of the $^{31}P\{^{1}H\}$ NMR spectra showed two major peaks at about 202 ppm, very close to the chemical shift region for the ^{31}P signals of the divalent imine-type complex **3** (ca. 201.9 ppm in DCM) and the analogous N-(Bn)H complex **4** shown in eq 3 (202.0 ppm in DCM). These assignments were confirmed later when we noted increases in the intensity of the corresponding NMR signals upon addition of authentic samples of each of **3** and **4** to solutions containing **1** and 1.2 equiv of NBS.

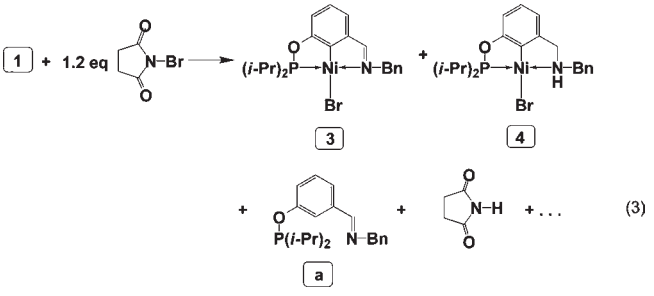

(3)

The ^{1}H NMR spectra recorded for samples containing 1 equiv each of NBS and **1** in dry C_6D_6 were also consistent with the formation of **3** (e.g., $PhCH_2N$ and $CH{=}N$ signals at about 4.9 and 7.3 ppm, respectively) and **4** (e.g., characteristic N*H* and $PhCH_2$ signals at 3.2−4.8 ppm). These spectra also contained the characteristic signals for succinimide and, curiously, the free ligand $PhCH_2N{=}CH(C_6H_4)OP(i\text{-}Pr)_2$ (eq 3). The next stage of the oxidation, which occurs when the reaction mixture contains more than 1 equiv of NBS, is characterized by a significant darkening of the sample and the gradual disappearance of all ^{31}P signals, implying the formation of paramagnetic species.

Detection of Oxidation Products by EPR Spectroscopy. While NMR provides insight into the diamagnetic products of the oxidation reaction, EPR can be used to detect the paramagnetic products. The samples used for the EPR measurements were prepared by dissolving different quantities of NBS in 0.22 mM toluene solutions of **1**. The resulting mixtures were kept at ambient temperature for approximately 10 min before being degassed by repeated freeze−pump−thaw cycles and cooled to 120 K in the EPR spectrometer. It is important to note that variations in mixing time or NBS content (up to 3 equiv) did not affect the EPR spectrum.

The EPR spectrum of the sample containing 1 equiv of NBS (Figure 3A) is typical of Ni^{III} pincer compounds possessing an axial bromine ligand.[14] In frozen solution, three of the four hyperfine components from the axial Br are visible as distinct peaks on the upfield end of the EPR spectra of such species; these features, indicated in Figure 3A, result from the large A_{zz} component of the splitting. As can be seen, the peak on the high field end is significantly broadened, probably as a result of dynamic hopping between two conformations. Because simulation of such dynamic effects increases the number of unknown parameters that must be fitted, we have chosen to perform a simpler simulation that includes only an anisotropic g-tensor and hyperfine coupling to one spin 3/2 nucleus; all other hyperfine couplings are simulated as an anisotropic Gaussian line width. The simulation shows that the g-tensor has principal values of $g_{xx} = g_{yy} = 2.22$ and $g_{zz} = 2.01$; arrows above the spectrum indicate the positions of features corresponding to these g-values. The hyperfine coupling constants to the spin 3/2 nucleus are found to be $A_{xx} = A_{yy} = 30$ G and $A_{zz} = 170$ G. The feature at ∼2950 G is the so-called "anomalous line" which occurs when one of the hyperfine components is similar in magnitude to the g-anisotropy.[15] The g-values and hyperfine couplings obtained from the simulation are consistent with a Ni^{III} complex possessing an axial Br ligand. Note that the simulation does not take the difference in magnetic moment between ^{79}Br and ^{81}Br into account and the reported couplings therefore represent an average of the coupling for the two isotopes. Additional smaller hyperfine splittings are visible in the experimental spectrum between ∼3250 and 3500 G indicating that the other atoms bound to the Ni^{III} center have non-zero nuclear spin.

The experimental and simulated EPR spectra for **2** (0.22 M solution in toluene, 120 K) are shown in Figure 3B. The similarity of spectra A and B in Figure 3 suggests that **2** is the main oxidation product observed in situ. However, careful inspection of the two spectra reveals some subtle differences. For example, the trough near ∼3100 G is shifted upfield in the spectrum of **2** by ∼20 G compared to the spectrum of the oxidation reaction mixture. This difference can be accounted for in the simulation by a small shift of the in-plane components of the g-tensor to $g_{xx} = 2.23$ and $g_{yy} = 2.19$. A slightly

dx.doi.org/10.1021/ic1025894 |*Inorg. Chem.* 2011, 50, 2661–2674

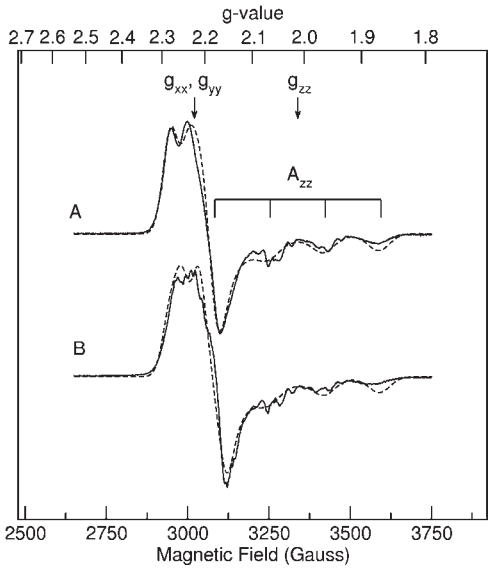

Figure 3. X-band (9 GHz) EPR spectra (toluene, 120 K) of the oxidation product(s) of **1** with 1 equiv of NBS (A) and compound **2** (B). The solid lines are experimental spectra, the dashed curves are simulations. Simulation parameters A: $g_{xx} = g_{yy} = 2.22$, $g_{zz} = 2.01$, $I = 3/2$ nucleus $A_{xx} = A_{yy} = 30$ G, $A_{zz} = 170$ G; B: $g_{xx} = 2.23$, $g_{yy} = 2.19$, $g_{zz} = 2.01$, $I = 3/2$ nucleus $A_{xx} = A_{yy} = 30$ G, $A_{zz} = 170$ G. Microwave frequency: 9.401599 GHz; microwave power: 2 mW; modulation amplitude: 1.0 G.

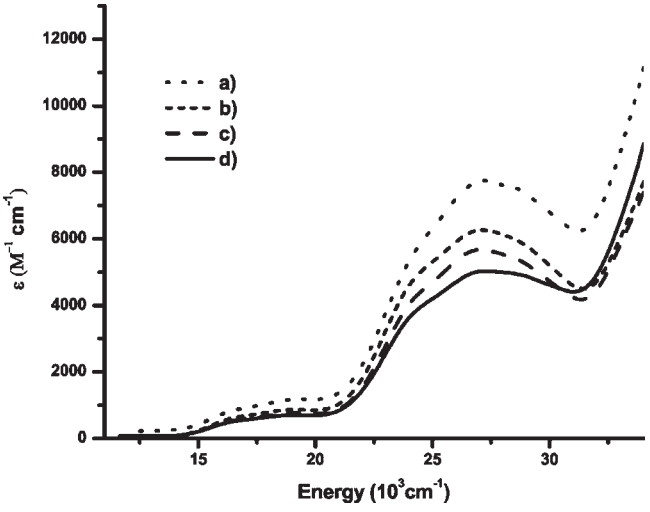

Figure 4. UV−vis spectra of nickel complexes (0.4 mM in DCM, 25 °C) with or without NBS: (a) **1** + 4 equiv of NBS; (b) **3** + **4** + 1.1 equiv of NBS; (c) complex **2** alone; (d) **4** + 1.1 equiv of NBS.

more pronounced hyperfine structure, probably due to Br, is also visible at ∼3000 G in the spectrum of **2**. The origin of these differences is uncertain but might be expected if the oxidation reaction mixture contained minor amounts of other Ni^{III} species. We note that the spectrum does not show evidence for any organic radicals indicating that any such species produced by the oxidation are unstable.

UV−vis Studies on Oxidation of Complexes 1, 3, and 4 with NBS. To complement the NMR and EPR studies discussed above, we have used UV−vis spectroscopy with the objective of identifying the paramagnetic intermediates/products

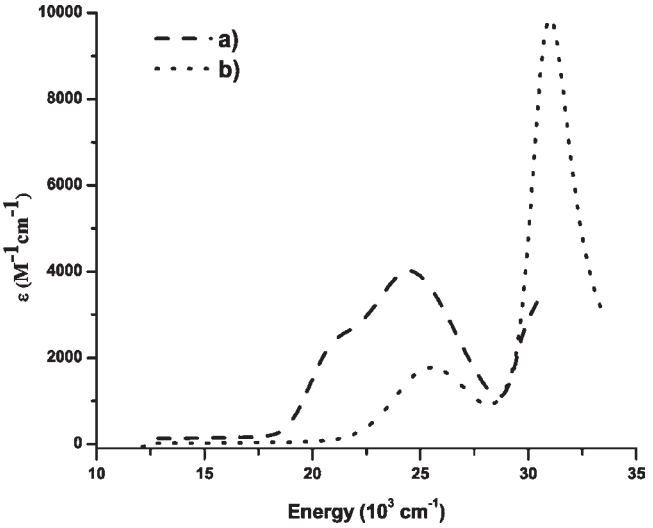

Figure 5. UV−vis spectra (25 °C) of the divalent complexes **3** (a) and **4** (b); both samples about 0.4 mM.

involved in the oxidation of **1**. UV−vis spectra were first recorded for all the complexes as well as the mixtures obtained from NBS oxidation of the divalent species to compare the spectral profiles to one another. Not unexpectedly, the spectrum of independently prepared **2** was virtually identical to the spectrum recorded for the mixture of **3** and NBS, and closely resembled the spectral profile of the mixture of **1** and NBS (Figure 4). Interestingly, a similar spectrum was also obtained for the mixture of **4** and NBS (Figure 4d), but in this case the oxidation product had a limited stability and decomposed over ∼5 min to an intractable green species. It is also noteworthy that under similar conditions the NBS oxidation proceeds much more rapidly for **1** and **4**. Finally, the spectra obtained for the trivalent complex **2** and the oxidation mixtures display multiple electronic transitions extending across the visible region (ca. 15000−28000 cm^{-1}, Figure 4), whereas the divalent complexes display absorption bands above about 20000 cm^{1} (Figures 1 and 5).

To monitor the course of the oxidation reaction, we titrated a 0.4 mM DCM solution of **1** (initial volume 2.50 mL) at ambient temperature with 50 μL aliquots of a 4 mM NBS solution, and the spectra were recorded 20 s after addition of each aliquot. The spectral profile for the entire titration (Figure 6) confirms the conclusions drawn from the NMR studies: the oxidation reaction takes place over two stages, each corresponding to the addition of 5−6 aliquots of NBS (approximately 1 equiv); beyond the 11-th aliquot (550 μL, ca. 2.1 equiv of NBS), the spectral profile remained fairly invariable and very similar to the absorption spectrum observed for complex **2** (Figure 4c).

Evolution of the spectral profile for the oxidation of **1** can be seen more clearly by examining the set of spectra corresponding to each of these two distinct stages of the titration. Thus, we can see in Figure 7 that addition of the first few aliquots of NBS results in a steady decrease in the intensities of the bands belonging to **1** (ca. 21000, 27500, and 31000 cm^{-1}), while a new band emerges gradually at about 24000−26000 cm^{-1}. Significantly, the absorbance remains fairly constant at about 26000 cm^{-1} during this stage of the reaction, but no clear isosbestic point was evident; this is consistent with the initial formation of an unstable intermediate.

dx.doi.org/10.1021/ic1025894 |*Inorg. Chem.* 2011, 50, 2661–2674

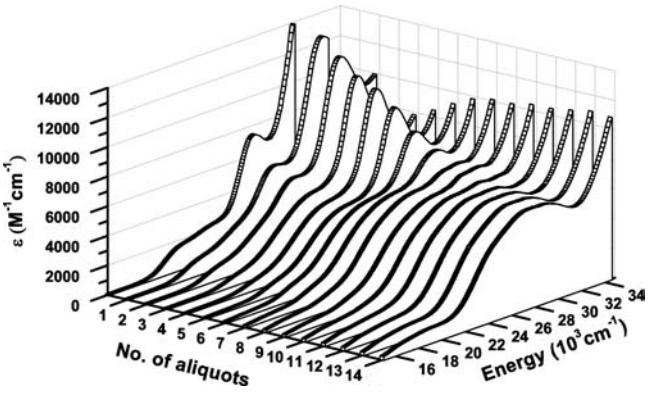

Figure 6. UV−vis spectra (25 °C) of **1** (2.5 mL of a 0.4 mM solution in DCM, spectrum 0) with 50 μL aliquots of a 4 mM solution of NBS in DCM (spectra 1−14).

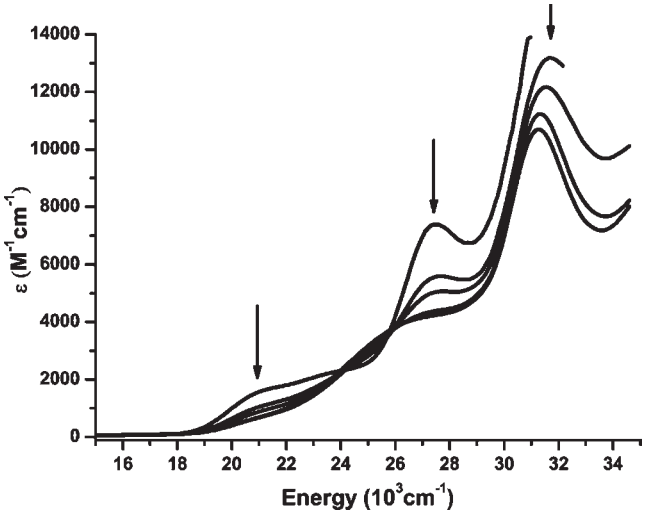

Figure 7. UV−vis spectra (25 °C) recorded during the initial stage of the titration of **1** with NBS. See main text for titration details.

Beyond the first equiv of NBS (>5 aliquots, Figure 8), there is a continued decline of the high-energy absorption at about 31000 cm^{-1} and a steady growth of multiple, poorly resolved bands at about 15000−20000 and 22000−27000 cm^{-1}. In contrast to what was observed in the first stage of the oxidation, a fairly clear isosbestic point is found during the second stage (at ca. 30000 cm^{-1}, Figure 8), implying a direct and intermediate-free transformation.

Computational Studies. Full molecular structures of **1** and $[\mathbf{1}]^{+\cdot}$ have been investigated using DFT at the B3LYP[16]/TZVP[17] level of the theory, their absorption spectra have been calculated using time-dependent DFT (TD-DFT),[18] and the results compared to the corresponding experimental data. These studies have corroborated the proposed (dimeric) structure of $[\mathbf{1}]^{+}$ and provided valuable details on the energies and compositions of the frontier molecular orbitals and spin density distribution in the open shell species arising from the oxidation of **1**, as described below.

Calculated Structures of 1 and $[1]^{+\cdot}$. The calculated structure of **1** is in very good agreement with the X-ray structure of this compound.[5j] For instance, the puckered (or cyclobutane-like) arrangement of the Ni_2N_2 core and the *syn* orientation of the

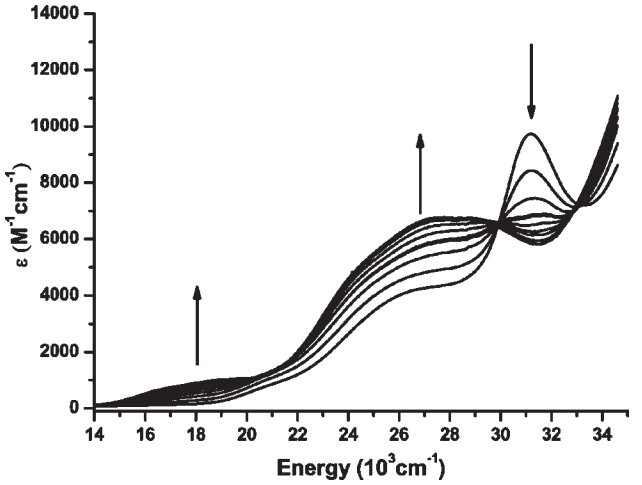

Figure 8. UV−vis spectra (25 °C) recorded during the second stage of the titration of **1** with NBS. See main text for titration details.

N-benzyl substituents observed in the X-ray structure of **1** are reproduced in the calculated structures; more specifically, the angle between two Ni_2N planes is 124° in the X-ray structure of **1** and 121.4° in the computed structures of **1** and $[\mathbf{1}]^{+\cdot}$. There is also good agreement between the experimentally observed (2.512(1) Å) and calculated (2.523 Å) Ni−Ni intermolecular distances in **1**; moreover, the computed Ni−Ni bond order (0.13)[19] indicates very little direct metal−metal interaction in this structure, as can be expected for low-spin d^8 Ni^{II} ions. On the other hand, a significantly shorter Ni−Ni distance (2.393 Å) and greater Ni−Ni bond order (0.43) were found in $[\mathbf{1}]^{+\cdot}$, resulting from the diminished occupancy (one electron) of the Ni−Ni σ^* orbital (Figure 9) in the oxidized species.

The shorter Ni−N distances in the X-ray and calculated structures of **1** correspond to the Ni and N atoms belonging to different halves of the dimer; this structural feature reflects the stronger covalence of the Ni−N bonds between different halves of the dimer (Ni−N bond order 0.56) versus those belonging to the same halves (Ni−N bond order 0.47). In the calculated structure of $[\mathbf{1}]^{+\cdot}$, the corresponding Ni−N bond orders are slightly greater (0.64 and 0.53, respectively) and the Ni−N distances are somewhat shorter (1.985/1.997 Å vs 2.006/2.027 Å). The opposite trend was observed for the Ni−C and Ni−P bonds, which were found to be the most covalent metal−ligand bonds (calculated bond orders 1.00 and 0.93, respectively). Thus, the calculated Ni−C distances were 1.885 Å in **1** (vs 1.864(2) Å in the X-ray structure) and 1.894 Å in $[\mathbf{1}]^{+\cdot}$; the corresponding Ni−P distances were 2.203 Å in **1** (vs 2.122(1) Å in the X-ray structure) and 2.268 Å in $[\mathbf{1}]^{+\cdot}$. These results can be understood in terms of HSAB theory: the greater compatibilities between a "softer" Ni^{II} ion in **1** (the atomic charge from natural population analysis (NPA)[20] +0.70 au) and "soft" phosphinite and aryl ligands should lead to more covalent bonds, while the "harder" character of the nickel ions in $[\mathbf{1}]^{+\cdot}$ (NPA-derived atomic charge +0.84 au) should favor stronger interactions with the "hard" amido ligands. Altogether, the valence index[21] for the Ni atoms is 3.16 in **1** and 3.74 in $[\mathbf{1}]^{+\cdot}$.

Inspection of the frontier molecular orbitals for **1** and $[\mathbf{1}]^{+\cdot}$ (Figures 9 and 10) and their compositions and energies (Table 1) has allowed us to evaluate the impact of oxidation on the electronic structure of **1** and to map out the spin density distribution in the oxidized species. Complete valence

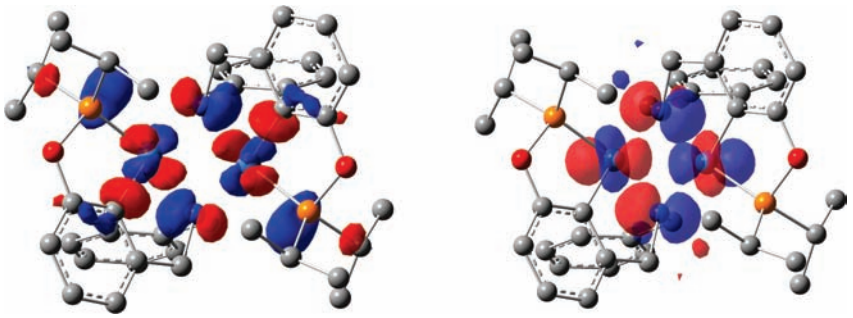

Figure 9. Frontier molecular orbitals of **1**: LUMO (left) and HOMO (right). Isosurface value of 0.04 au for both orbitals. Spheres are colored to signify the atoms in keeping with convention: gray for carbon, blue for nitrogen, orange for phosphorus, red for oxygen, light-blue for nickel. H atoms are not shown for clarity.

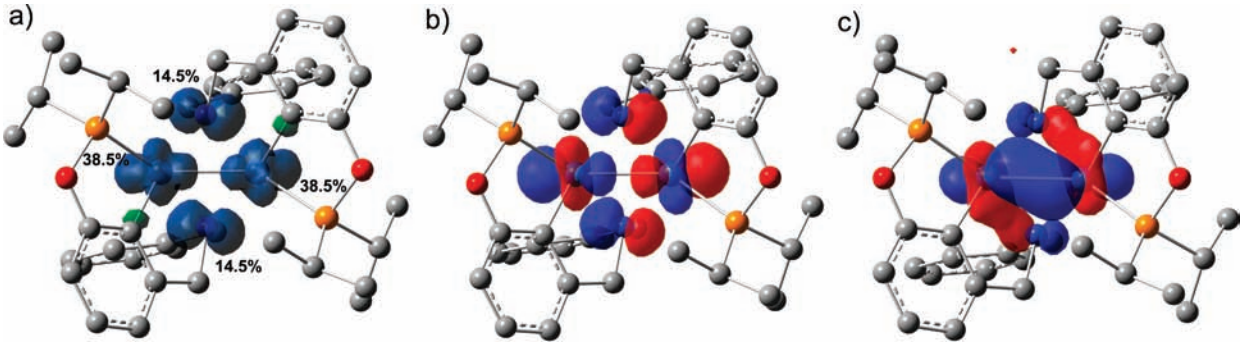

Figure 10. Spin density and frontier molecular orbitals of $[\mathbf{1}]^{+\cdot}$: (a) spin density (isosurface value of 0.004 au), (b) β-spin LUMO (isosurface value of 0.04 au), and (c) β-spin HOMO-10 (isosurface value of 0.04 au). Spheres are colored to signify the atoms in keeping with convention: gray for carbon, blue for nitrogen, orange for phosphorus, red for oxygen, light-blue for nickel. H atoms are not shown for clarity. In Figure 10a, blue and green colors indicate positive (α) and negative (β) spin density, respectively.

delocalization of the Ni_2N_2 core in $[\mathbf{1}]^{+\cdot}$ is implied from the symmetrical spin density distribution (0.77 e^- from two Ni atoms and 0.29 e^- from two bridging N atoms, Figure 10a);[22] therefore, complex $[\mathbf{1}]^{+\cdot}$ represents a class III mixed-valence system[23] ($Ni^{+2.5}{}_2N_2$) analogously to the oxidized binuclear Cu_A center in bioinorganic chemistry ($Cu^{+1.5}{}_2S_2$).[4b,4h] The observation of symmetrical spin density distribution in these bimetallic systems stands in contrast to the localized spin density distribution reported for $[LNi^{II}Ni^{III}(NCCH_3)_2]^{3+}$ (Chart 1).[8]

To probe the influence of axial ligation on spin density distribution in our system, we constructed a smaller model featuring *N*-Me substituents and performed structure optimization for oxidized species bearing either an axial Br ligand attached to one Ni, $(\mu\text{-L})_2Ni_2Br$, or a positive charge (analogously to $[\mathbf{1}]^{+\cdot}$). Analysis of the electronic structures of these models showed that the latter species has a more symmetrical spin density distribution on the Ni_2N_2 core: 0.26 e^- on each N and 0.23 e^- on each Ni. In contrast, the spin density distribution is entirely localized on the Ni−Br_{ax} moiety of the neutral species $(\mu\text{-L})_2Ni_2Br$, with 0.82 e^- on Ni (d_{z^2}) and 0.20 e^- on Br (p_z), which implies that the bimetallic core in this species can best be described as $BrNi^{III}N_2Ni^{II}$. The Ni−Br_{ax} bond in this model was found to be quite long (2.547 Å), which is anticipated on the basis of theoretical considerations and consistent with experimental values observed in X-ray structures of related pentacoordinate, 17-electron complexes (pincer)$NiBr_2$ (Ni−Br_{ax}∼2.43−2.46 Å).[5e−5i] It appears, therefore, that the spin distribution in these dinickel complexes is highly sensitive toward changes in the ligand environment around the Ni ions. This is in sharp contrast to behavior of systems with the softer Cu_2S_2 core where high covalency of Cu-thiolate bonds ensures high stability of spin distribution.[4h]

Table 1. Frontier Molecular Orbital Energies and Compositions (%) for 1 and $[\mathbf{1}]^{+\cdot}$

	energy (eV)	Ni	N	P
1				
LUMO+2	−0.49	16	3	18
LUMO+1	−0.86	44	10	23
LUMO	−1.12	40	11	21
HOMO	**-5.08**	**55**	**28**	**2**
HOMO-3	−5.70	71	10	4
HOMO-9	−6.47	77	10	5
$[\mathbf{1}]^+$				
***β*-LUMO**	**-6.57**	**68**	**20**	**3**
β-HOMO	−8.72	7	0	1
β-HOMO-1	−8.81	8	0	1
β-HOMO-2	−8.97	0	0	0
β-HOMO-3	−8.98	17	10	0
β-HOMO-7	−9.28	3	3	0
β-HOMO-10	−9.63	85	13	1
β-HOMO-13	−10.36	72	9	3

Calculated Absorption Spectra for 1 and $[\mathbf{1}]^{+\cdot}$. The calculated spectra for **1** and $[\mathbf{1}]^{+\cdot}$ are depicted in Figure 11, while

dx.doi.org/10.1021/ic1025894 |*Inorg. Chem.* 2011, 50, 2661–2674

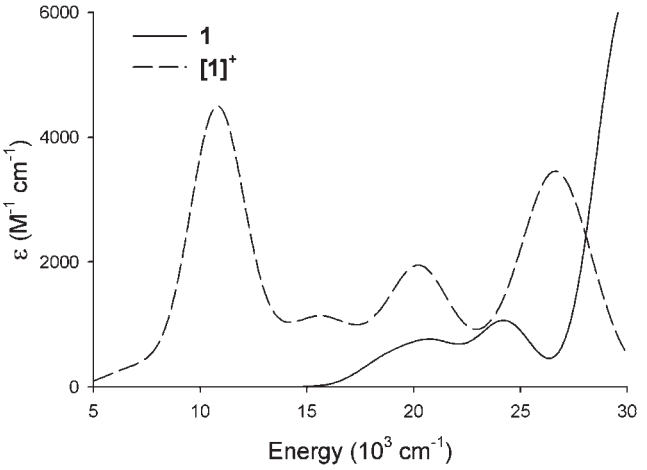

Figure 11. TD-DFT-calculated visible absorption spectra of **1** (solid line) and $[\mathbf{1}]^{+\cdot}$ (dash line), calculated at the B3LYP/TZVP level of theory.

the spectral details (energies, probabilities, and assignments of bands) are listed in Table 2. The lowest-energy, spin-allowed absorption transition found in the predicted spectrum for **1** at 18,700 cm^{-1} is due principally to an electronic transition from the metal-based HOMO to the metal-based LUMO. This transition overlaps with two other transitions, a weak HOMO→LUMO+1 transition at 19000 cm^{-1} and a stronger HOMO-3→LUMO transition at 21000 cm^{-1}, to form a single band at 20500 cm^{-1} with a shoulder at 18,700 cm^{-1}. The second intense band (at 24300 cm^{-1}) is due to the HOMO-9→LUMO transition. For comparison, the corresponding transitions in the experimental spectrum of **1** are manifested by poorly resolved bands at about 19000−21000 and 22500−25000 cm^{-1}, respectively (Figure 2a). In all these transitions, the donor and acceptor orbitals are located primarily on the Ni_2N_2 cluster. A very intense band due to the HOMO→LUMO+2 (π^*) transition is also present in the predicted and experimental spectra, at 29,600 and about 27500 cm^{-1}, respectively.

Recall that conversion of **1** to $[\mathbf{1}]^{+\cdot}$ involves the removal of an electron from the HOMO (Figure 9) and generation of a $(\sigma^*)^1$ ground state configuration featuring a low-energy vacant orbital (β-spin LUMO, Figure 10b). This leads to low-energy transitions from the fully occupied orbitals to the β-spin LUMO, these transitions appearing in the near-IR and visible regions of the absorption spectrum of $[\mathbf{1}]^{+\cdot}$ (Figure 11, Table 2). The transition from the bonding β-spin HOMO−10 (Ni d_{z^2} + d_{z^2}, Figure 10c) to the β-spin LUMO is the main component of the intense absorption band at 10,800 cm^{-1} in the predicted spectrum of $[\mathbf{1}]^{+\cdot}$, but a few minor contributions are also found for this transition (Table 2).

Characterization of 2 and 3 by NMR and X-ray Diffraction Analyses. Complete characterization of the dimeric complex **1** and its monomeric precursor **4** has been described previously. This section describes the characterization of complexes **2** and **3** by single crystal X-ray crystallography and elemental analysis; paramagnetic **2** was also analyzed by EPR studies (vide supra), while the diamagnetic complex **3** was characterized by NMR spectroscopy. The ^{31}P $\{^1H\}$ NMR spectrum of **3** (C_6D_6) displays a singlet at 201.4 ppm (201.9 ppm in DCM), downfield of the signals for the free ligand (149 ppm) and **1** (191.6 ppm), and very close to the corresponding signal for complex **4** (201.7 ppm in C_6D_6, 202.0 ppm in DCM). The ^1H NMR of this sample showed a singlet at about 4.9 ppm for $PhC\underline{H}_2N$ and a doublet at about 7.3 ppm for $C\underline{H}$═NBn ($^4J_{H-P}$ = 4 Hz), whereas the ^{13}C $\{^1H\}$ NMR spectrum showed a doublet at about 172 ppm for $C\underline{H}$═N ($^3J_{C-P}$ = 3 Hz). As expected, fresh samples of **2** were NMR silent, but over time the signal corresponding to **3** was detected in the $^{31}P\{^1H\}$ NMR spectrum of **2**, indicating that the trivalent species **2** undergoes thermal decomposition to form its divalent analogue (eq 4).

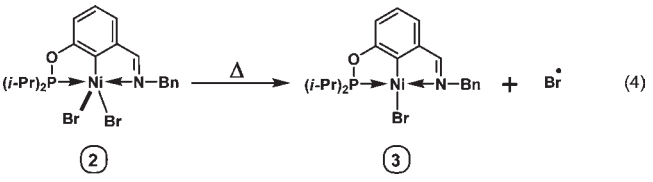

(4)

Suitable single crystals were obtained for complexes **2** and **3** and subjected to single crystal diffraction analyses; the ORTEP diagrams are shown in Figure 12, and selected crystal data and

Table 2. Spin-Allowed Absorption Bands Calculated for 1 and $[\mathbf{1}]^{+\cdot}$[a]

1			$[\mathbf{1}]^{+\cdot}$		
energy (cm^{-1})	f[b]	assignment	energy (cm^{-1})	f[b]	assignment
18700	0.0046	HOMO→ LUMO (56%)	6400	0.0003	β-HOMO-4→ LUMO (55%)
19000	0.0010	HOMO→ LUMO+1 (58%)	6700	0.0027	β-HOMO-3→ LUMO (55%)
21000	0.0081	HOMO-3→ LUMO (35%)	8000	0.0019	β-HOMO-13→ LUMO (31%)
					β-HOMO-10→ LUMO (30%)
24300	0.0143	HOMO-9→ LUMO (25%)	10800	0.0596	β-HOMO-10→ LUMO (38%)
29600	0.0611	HOMO→ LUMO+2 (74%)	11500	0.0020	β-HOMO-12→ LUMO (64%)
			13500	0.0047	β-HOMO-2→ LUMO (28%)
					β-HOMO→ LUMO (25%)
			14300	0.0020	β-HOMO-2→ LUMO (66%)
			15500	0.0090	β-HOMO-7→ LUMO (22%)
					β-HOMO-13→ LUMO (21%)

[a] Transitions in the near-IR, visible, and near-UV region (6000−30000 cm^{-1} for **1** and up to 16000 cm^{-1} for $[\mathbf{1}]^+$), calculated at the B3LYP/TZVP level of theory. Excitation contributions greater than 10% are shown, smaller contributions are omitted. [b] f = oscillator strength. The complete list of calculated transitions can be found in the Supporting Information.

dx.doi.org/10.1021/ic1025894 |*Inorg. Chem.* 2011, 50, 2661–2674

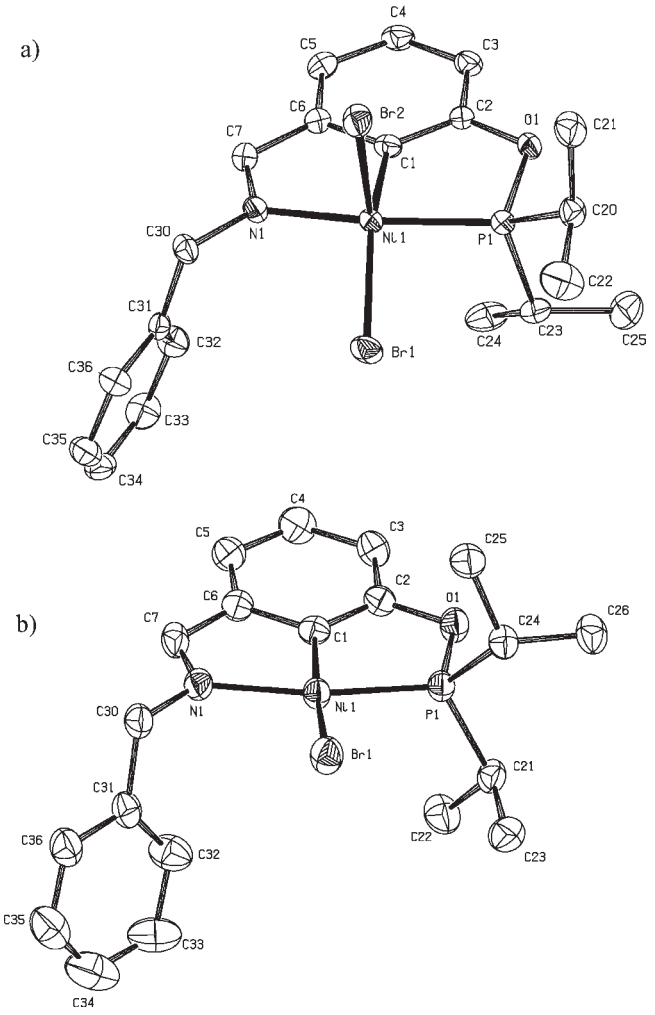

Figure 12. ORTEP diagrams for complexes **2** (a) and **3** (b). Thermal ellipsoids are set at the 50% probability level. Hydrogen atoms are omitted for clarity.

structural parameters are listed in Tables 3 and 4. The nickel center in complex **3** adopts a nearly perfect square planar geometry, thanks to the planar configuration adopted by the CH=NBn moiety. The sp^2-hybridized and less sterically encumbered imine moiety also forms a shorter bond to the Ni center in comparison to the corresponding distance in previously reported POCN-type complexes featuring amine moieties (1.990 vs ca. 2.030 Å).[5i] Complex **2** displays a square pyramidal geometry where the phosphinito moiety is slightly outside of the plane defined by the atoms C, Ni, and N and the aromatic ring; this is a generally observed deformation in pentacoordinated complexes of Ni^{III} that can be attributed to the partially filled d_{z^2} orbital and steric repulsions between the P-substituents and the lone pairs of the axial bromine atom. A slight pyramidal distortion is also apparent from (a) the out-of-plane displacement of the Ni center in **2** (by ca. 0.35 Å) from the basal plane defined by the atoms P1, C1, N1, and Br1, and (b) the C(1)−Ni-Br(1) angle that is much smaller in **2** than **3** (155° vs 171°). Moreover, the pentacoordinate Ni^{III} center forms significantly longer bonds with C1, P, and the axial Br. Similar pyramidal distortions and stretched bonds were also observed when divalent (POCN)NiBr was converted into the trivalent complexes $(POCN)NiBr_2$.[5i]

CONCLUSIONS

The study reported herein has provided a survey of the oxidation pathways traversed by complex **1**, a rather rare dimeric compound featuring two Ni^{II} centers held by pincer ligands at sufficiently close proximity to allow electronic interactions. The results described above have demonstrated that electrolytic oxidation converts **1** to a radical cation that appears to maintain the original dimeric structure; in contrast, chemically induced oxidation converts **1** to an unstable intermediate species that decomposes to give, eventually, the monomeric product **2** featuring a trivalent Ni center and an oxidized (imine-type) new ligand (Scheme 2).

NMR and UV−vis monitoring of the reaction of **1** with NBS revealed the formation of succinimide and two monomeric divalent species, **3** and **4**, that are among the intermediates generated in the chemical oxidation of **1**. The independent synthesis and full characterization of complex **3**, and its direct oxidation to **2**, provided further support for the postulated pathway shown in Scheme 2. On the other hand, the initial product of the reaction of **1** with NBS, species **A** in Scheme 2, could not be detected. The postulated structure of this species involves formal oxidation at one Ni center and the concomitant formation of a Ni−Br bond; this proposal is based on the observed tendency of POCN-type pincer complexes of nickel complexes to undergo one-electron oxidation at the nickel center as opposed to the ligand.[24]

Another ambiguous aspect of the chemical oxidation of **1** touches on whether succinimide is generated via H-abstraction from the solvent or from the $ArCH_2$ moiety in the postulated intermediates **A**. One argument against the prevalence of the latter pathway is that succinimide is also generated in the conversion of (POCN)NiBr to $(POCN)NiBr_2$ with no concomitant oxidation of the POCN ligand.[5j] It is tempting to argue that succinimide is generated by the H-abstraction from the reaction medium, and to propose a hydrogen transfer mechanism from one $ArCH_2N$ moiety in **A** to another, thus generating the CH=NBn moiety in **3** and the N*H* moiety in **4**, but other possibilities can not be ruled out.

The results obtained from cyclic voltammetry and spectroelectrochemical measurements as well as computational investigations have allowed us to survey the redox and absorption properties of **1** and compare them to the corresponding data reported for monomeric species $(POCN)NiBr_{2/3}$ and related dinickel species $[LNi_2]^{2+/3+}$ and $[LNi_2(NCCH_3)_2]^{3+}$ (L is a "compartmental macrocyclic ligand" shown in Chart 1). When combined together, these results point out that electrolytic oxidation of **1** removes an electron from the HOMO to generate a dimeric radical cation, $[\mathbf{1}]^{+\cdot}$. Since the HOMO in **1** has antibonding character with respect to the Ni−Ni bond, formation of $[\mathbf{1}]^{+\cdot}$ brings about greater Ni−Ni bond order in $[\mathbf{1}]^{+\cdot}$. DFT studies have established that the experimentally observed and computationally predicted low-energy electronic transitions extending into the near-IR region originate from the presence of low-lying β-LUMO in $[\mathbf{1}]^{+\cdot}$.

Another important question addressed by the current study pertains to the localization of the spin density on metal centers and ligand atoms. Previous studies have shown that the spin density in the open shell monomeric pincer complexes $(POCN)NiBr_2$,[5i] $(POCOP)NiX_2$,[5e,5f] and $(PCP)NiX_2$[5g] is entirely localized on the $Ni-Br_{ax}$ moiety, as was found to be the case in complex **2**. In the case of the dinickel species

dx.doi.org/10.1021/ic1025894 |*Inorg. Chem.* 2011, 50, 2661–2674

Table 3. Crystal Data Collection and Refinement Parameters for Complexes 2 and 3

	2	3
chemical formula	$C_{20}H_{25}NiPNOBr_2$	$C_{20}H_{25}NiPNOBr$
Fw	546.93	464.99
T (K)	150	150
wavelength (Å)	0.71073	1.54178
space group	$P2_1/n$	$P2_1/c$
a (Å)	8.4257(8)	10.0435(2)
b (Å)	26.053(3)	42.5527(7)
c (Å)	10.051(1)	14.9885(2)
α (deg)	90	90
β (deg)	106.6550(1)	107.425(1)
γ (deg)	90	90
Z	4	12(Z′ = 3)
V (Å^3)	2113.8(4)	6111.79(2)
ρ_{calcd} (g cm^{-3})	1.719	1.584
μ (cm^{-1})	47.84	45.14
θ range (deg)	1.56−27.54	2.08−72.78
R1[a] [$I > 2\sigma(I)$]	0.0208	0.0656
wR2[b] [$I > 2\sigma(I)$]	0.0450	0.1641
R1 [all data]	0.0288	0.0688
wR2 [all data]	0.0464	0.1658
GOF	0.959	1.139

[a] $R_1 = \sum||F_o| - |F_c||/\sum|F_o|$. [b] $wR_2 = \{\sum w(F_o^2 - F_c^2)^2/\sum w(F_o^2)^2\}^{1/2}$.

Table 4. Selected Bond Distances (Å) and Angles (deg) for Complexes 2 and 3

parameter	2	3
Ni−C(1)	1.896(2)	1.860(5)
Ni−P	2.1919(5)	2.125(2)
Ni−N	2.004(2)	1.990(5)
Ni−Br(1)	2.3597(4)	2.338(1)
Ni−Br(2)	2.4191(3)	
C(1)−Ni−Br(1)	155.43(5)	171.1(2)
C(1)−Ni−Br(2)	95.92(5)	
P−Ni−N	158.25(5)	162.7(2)
N−Ni−Br(1)	100.17(4)	100.2(2)
P−Ni−Br(1)	92.99(2)	97.11(5)
N−Ni−Br(2)	93.14(4)	
P−Ni−Br(2)	99.13(2)	
P−Ni−C(1)	78.43(6)	80.3(2)
N−Ni−C(1)	82.52(7)	82.6(2)

$[LNi^{II}Ni^{III}(NCCH_3)_2]^{3+}$, DFT studies have shown that most of the spin density is localized on the six coordinate Ni ion (72% on $3d_{z^2}$ and 16% on $3d_{xy}$) as well as the N atoms of the acetonitrile moieties coordinated to it (ca. 15%).[8] Similarly, a DFT analysis has shown that the presence of an axial Br in our system would localize the spin on the Ni−Br_{ax} moiety, giving a $BrNi^{III}Ni^{II}N_2$ core; this might explain the diminished thermal stability of the chemical oxidation intermediate A illustrated in Scheme 2. In contrast, computational analysis of $[\mathbf{1}]^{+\cdot}$ (no axial ligands, *N*-Me or *N*-Bn substitutents) has revealed a delocalization of spin density over the Ni_2N_2 core, with a substantial amount of spin density residing over the two N atoms. We conclude that $[\mathbf{1}]^{+\cdot}$ is best described as a weighted average of two limiting resonance structures (Chart 2) featuring (a) anionic amide moieties and $Ni^{+2.5}$ centers (left-side illustration), and (b) an amide moiety and an aminyl radical delocalized through the two Ni^{II} centers (right-side illustration). Thus, the amide-type POCN ligand in **1** can be considered a new example of the non-innocent pincer ligands introduced by Grützmacher's[25] and Mindiola's[26] groups.[27]

The unanticipated conversion of the dimeric complex **1** into the monomeric 17-electron complex **2** featuring a new imine-type POCN ligand and the successful, high-yield synthesis of this species have opened up a new avenue for further exploration of its reactivities, including the possible promotion of radical addition and cyclization reactions. Future studies will probe these reactivities.

EXPERIMENTAL SECTION

General Procedures. All manipulations were carried out using standard Schlenk and glovebox techniques under nitrogen atmosphere. All solvents used for experiments were dried to water content of less than 10 ppm by passage through activated aluminum oxide (MBraun SPS) and deoxygenated by vacuum-nitrogen extraction. C_6D_6 was dried over molecular sieves (pore size 4 Å) and then deoxygenated by 3−5 freeze−pump−thaw cycles. The quality of the solvents used for experiments was tested using a Mettler Toledo C20 coulometric Karl Fischer titrator. The following were purchased from Aldrich and used without further purification: Ni (metal), chlorodiisopropylphosphine, N-Bromosuccinimide, 3-hydroxybenzaldehyde, triethylamine, and C_6D_6. A Bruker AV 400 spectrometer was used for recording ^{1}H, ^{13}C{^{1}H} (101 MHz), and ^{31}P{^{1}H} (162 MHz). ^{1}H and ^{13}C chemical shifts are reported in parts per million (ppm) downfield of TMS and referenced against the residual C_6D_6 signals (7.15 ppm for ^{1}H and 128.02 ppm for ^{13}C); ^{31}P chemical shifts are reported in ppm and referenced against the signal for 85% H_3PO_4 (external standard, 0 ppm). Coupling constants are reported in hertz (Hz). The correlation and assignment of ^{1}H and ^{13}C NMR resonances were aided by ^{1}H COSY, HMQC, and DEPT. UV−vis spectra were recorded on Varian Bio 300 equipped with a temperature controlling system using standard sampling cells (1 cm optical path length). The spectroelectrochemical cell used for the spectroelectrochemical studies was purchased from CH Instruments, Inc. 3700 Tennison Hill Drive, Austin, TX 78738 U.S.A. (www.chinstruments.com).

Synthesis of the $\kappa^P,\kappa^C,\kappa^N$-{2,6-(*i*-$Pr_2$PO)($C_6H_3$)(CH=NBn)}-$NiBr_2$ (2). *Method A.* To a solution of **1** (200 mg, 0.260 mmol) in 5 mL of dry and degassed DCM cooled to −78 °C was added 181 mg of NBS (1.04 mmol). The resulting dark brown-black mixture was allowed to stir for additional 5 min and then treated with 5 mL of cold hexane, followed by filtration of the formed precipitate. The solvent was reduced to approximately 2 mL in vacuum, and the resulting mixture was left to crystallize at −18 °C for approximately one week. Black crystals were collected, washed with cold hexane, and dried under vacuum for 1 h to furnish **2** (64 mg, 23%).

Method B. To the solution of **3** in 5 mL of dry and degassed DCM at −78 °C was added a DCM solution of Br_2 (2 mL, 0.059 mM). The resulting dark brown-black mixture was allowed to stir for additional 5 min, and then the solvent was removed under vacuum to give a dark purple-black powder (0.110 g, 94%).

Anal. Calcd for $C_{20}H_{25}OPNNiBr_2$: C, 44.08; H, 4.62; N, 2.57; Found: C, 43.89; H, 4.77; N, 2.66.

Synthesis of the 3-((Benzylimino)methyl)phenol (a). To a solution of 3-hydroxybenzaldehyde (1.00 g, 8.20 mmol) in 10 mL of

dx.doi.org/10.1021/ic1025894 |*Inorg. Chem.* 2011, 50, 2661–2674

Scheme 2

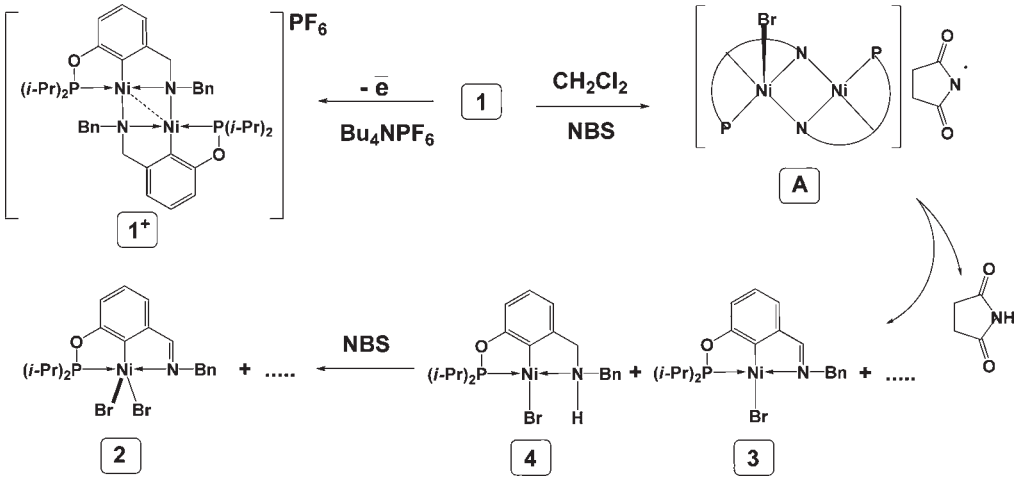

Chart 2

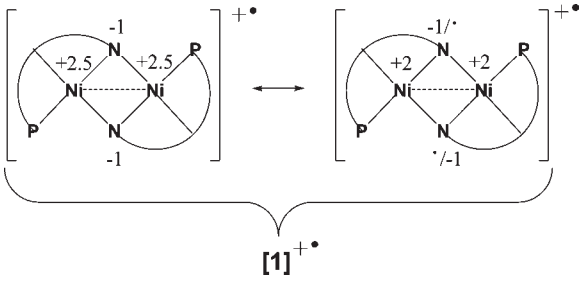

methanol at room temperature (r.t.) was added a solution of benzylamine (0.880 g, 8.20 mmol) in 10 mL of methanol. The resulting mixture was stirred for 1 h to obtain the anticipated Schiff base as a white suspension. Removal of volatiles under vacuum for 1 h gave **a** as a white powder (1.68 g, 97%). ^{1}H NMR (δ, $CDCl_3$): 4.75 (s, 2H, Bn{CH_2}), 6.84 (d, ^3J = 7, 1H, {Ar}H^6), 7.15−7.23 (m, 3H), 7.23−7.31 (m, 5H, overlapping with $CHCl_3$), 8.23 (s, 1H, CH═N). ^{13}C{^{1}H} NMR (δ, $CDCl_3$): 64.83 (s, 1C, CH_2Ph), 114.13 (s, 1C, {Ar}C^6), 118.70 (s, 1C, {Ar}C^2), 121.72 (s, 1C, {Ar}C^4), 127.30 (s, 1C, {Ar}C^5), 128.25 (s, 2C, {Bn}C^{meta}), 128.71 (s, 2C, {Bn}C^{ortho}), 130.04 (s, 1C, {Bn}C^{para}), 137.32 (s, 1C, {Bn}C^{ipso}), 138.86 (s, 1C, {Ar}C^3), 156.43 (s, 1C, {Ar}C^1), 162.58 (s, 1C, CH═N).

Synthesis of the 3-((Benzylimino)methyl)(phosphinito)-benzene (b). To a solution of **a** (1.00 g, 4.73 mmol) and triethylamine (0.788 mL, 5.20 mmol) in THF (35 mL) stirring at 0−5 °C was added chlorodiisopropyl phosphine (96% assay, 0.780 mL, 4.73 mmol). The resulting mixture was allowed to warm to room temperature, stirred for an additional hour, and evaporated under decreased pressure to give an oily residue, which was extracted with hexane (3 × 25 mL). Evaporation of the combined extracts furnished the product as a colorless oil (1.47 g, 95%). ^{1}H NMR (δ, C_6D_6): 0.94 (dd, $^3J_{HH}$ = 7, $^3J_{HP}$ = 16, 6H, $CHCH_3$), 1.10 (dd, $^3J_{HH}$ = 7, $^3J_{HP}$ = 11, 6H, $CHCH_3$), 1.85−1.60 (m, 2H, $CHCH_3$), 4.56 (s, 2H, {Bn}CH_2), 7.12−7.04 (m, 2H, {Ar}H^5 and {Bn}H^{para}), 7.17 (t, $^3J_{HH}$ = 6, 2H, {Bn}H^{meta}), 7.32−7.23 (m, 3H, {Ar}H^6 and {Bn}H^{para}), 7.37 (d, $^3J_{HH}$ = 8, 1H, {Ar}H^4), 7.95 (br s, 2H, {Ar}H^2 and CH═N). ^{13}C{^{1}H} NMR (δ, C_6D_6): 17.14 (d, $^2J_{CP}$ = 9, 2C, $CHCH_3$), 17.82 (d, $^2J_{CP}$ = 20, 2C, $CHCH_3$), 28.60 (d, $^1J_{CP}$ = 18, 2C, $CHCH_3$), 65.14 (s, 1C, {Bn}CH_2), 118.27 (d, $^3J_{CP}$ = 11, 1C, {Ar}C^6), 121.08 (d, $^3J_{CP}$ = 11, 1C, {Ar}C^6), 122.41 (s, 1C, {Ar}C^4), 127.04 (s, 1C, {Ar}C^5), 128.27 (s, 2C, {Bn}C^{ortho}), 128.68 (s, 2C, {Bn}C^{meta}), 129.83 (s, 1C, {Bn}C^{para}), 138.69 (s, 1C, {Bn}C^{ipso}), 140.21 (s, 1C, {Ar}C^3), 160.27 (d, J_{CP} = 9, 1C, {Ar}C^3), 161.20 (s, 1C, CH═N). ^{31}P{^{1}H} NMR (δ, C_6D_6): 148.7 (s, 1P).

Synthesis of the $\kappa^P,\kappa^C,\kappa^N$-{2,6-($i$-Pr$_2$PO)($C_6H_3$)(CH═NBn)}NiBr (3). A solution of **b** (1.47 g, 4.49 mmol) in 20 mL of benzene was slowly added to the stirring suspension of $NiBr_2(CH_3CN)_x$ (1.350 g, 4.49 mmol) and triethylamine (0.625 mL, 4.49 mmol) in toluene (15 mL) at r. t. The resulting dark brown mixture was then heated for 5 h at 60 °C. Removal of the solvent and purification of the solid residues by column chromatography (SiO_2, eluents: hexane followed by 70:30 CH_2Cl_2/Hexane) furnished the product as a brick-red powder (2.08 g, 89%).

^{1}H NMR (δ, C_6D_6): 1.12 (dd, $^3J_{HH}$ = 7, $^3J_{HP}$ =15, 6H, 2 × $CHCH_3$), 1.41 (dd, $^3J_{HH}$ = 7, $^3J_{HP}$ =18, 6H, 2 × $CHCH_3$), 2.28−2.03 (m, 2H, 2 × $CHCH_3$), 4.90 (s, 2H, {Bn}CH_2), 6.41 (d, $^3J_{HH}$ = 7, 1H, {Ar}H^5), 6.60 (d, $^3J_{HH}$ = 8, 1H, {Ar}H^3), 6.70 (t, $^3J_{HH}$ = 8, 1H, {Ar}H^4), 7.02 (t, $^3J_{HH}$ = 7, 1H, {Bn}H^{para}), 7.09 (t, $^3J_{HH}$ = 7, 2H, 2 × {Bn}H^{ortho}), 7.21 (d, $^3J_{HH}$ = 7, 2H, 2 × {Bn}H^{meta}), 7.29 (d, $^3J_{HP}$ = 4, 1H, CH═N). ^{13}C{^{1}H} NMR (δ, C_6D_6): 16.76 (d, $^2J_{CP}$ = 2, 2C, $CHCH_3$), 18.08 (d, $^2J_{CP}$ = 4, 2C, $CHCH_3$), 28.79 (d, ^1J = 23, 2C, $CHCH_3$), 60.09 (s, 1C, {Bn}CH_2), 113.14 (d, J = 12, 1C, {Ar}C^3), 120.91 (d, ^4J = 2, {Ar}C^5), 126.51 (s, 1C, {Ar}C^4), 127.71 (s, 1C, {Bn}C^{para}), 128.88 (s, 2C, 2 × {Bn}C^{ortho}), 129.65 (s, 2C, 2 × {Bn}C^{meta}), 138.15 (s, 1C, {Bn}C^{ipso}), 148.3 (s, 1C, {Ar}C^6), 153.40 (d, ^2J = 35, 1C,{Ar}C^1), 165.76 (d, ^2J = 10, 1C, {Ar}C^2), 172.18 (d, ^2J = 3, 1C, CH═N). ^{31}P{^{1}H} NMR (δ, C_6D_6): 201.35 (s, 1P).

Anal. Calcd for $C_{20}H_{25}OPNNiBr$: C, 51.66; H, 5.42; N, 3.01; Found: C, 51.55; H, 5.59; N, 3.08.

Electrochemical Studies. Cyclic voltammetry measurements were performed on a BAS Epsilon potentiostat at room temperature using deoxygenated DCM solutions of the sample and a standard three electrode system consisting of a glassy carbon working electrode, a Pt auxiliary electrode, and a Ag/AgCl reference electrode. Bu_4NPF_6 was used as supporting electrolyte (0.1 M). Under these conditions, Ferrocene showed a reversible redox wave at $E^0_{1/2}$= +0.48 V, which serves as the reference point for all redox potentials quoted in this report.

The spectroelectrochemical (SEC) measurements on complex **1** were performed at room temperature using a Varian 500 UV−vis−NIR spectrometer in combination with a BAS Epsilon potentiostat in DCM solutions containing (n-Bu)$_4$NPF$_6$ (0.1 M). The experiments were carried out on a three electrode setup consisting of a 5 mm diameter platinum

dx.doi.org/10.1021/ic1025894 |Inorg. Chem. 2011, 50, 2661–2674

mesh electrode as working electrode, a platinum wire counter electrode, and an Ag/AgCl reference electrode, and using micro sampling cells with a 1 mm optical path length. The chemical reversibility of all processes was confirmed by reversing the applied potential (from 0.07 V to −0.25 V) and regenerating the spectrum of the starting complex **1**. The spectrum shown in Figure 2 was obtained at the end of the oxidative electrolysis.

EPR Spectroscopy. EPR spectra were collected on a Bruker Elexsys E580 spectrometer operating in cw mode. For compound 2, a solution (~0.5 mM) in toluene was prepared, and placed in a 4 mm o.d. EPR tube. The solution was then degassed by repeated freeze−pump−thaw cycles, and the tube was sealed under vacuum. The sample was frozen to 120 K in the spectrometer resonator. For the oxidation of **1**, a solution of **1** (0.67 mM) was mixed with a solution of NBS (6.7 mM) in DCM in the volume ratio needed to give the desired mole ratio and diluted to give a final concentration of **1** of 0.22 mM.

Computational Details. All DFT calculations were performed using the Gaussian 09 package.[28] Stationary points on the potential energy surface were obtained using the B3LYP hybrid density functional.[16] Geometry optimizations were performed using the TZVP basis set[17] for all atoms. Tight SCF convergence criteria were used for all calculations. Symmetry was not used in the calculations. The converged wave functions were tested to confirm that they correspond to the ground-state potential energy surface. Mayer bond orders[29] and the analysis of molecular orbitals in terms of fragment orbital contributions were carried out using the AOMix program.[30] Absorption spectra were calculated from time-dependent DFT (TD-DFT)[18] simulations at the B3LYP/TZVP level. Calculated excitation energies and oscillator strengths were converted into absorption spectra using the pseudo-Voigt functions (50% Gaussian and 50% Lorentzian) and the 3000 cm^{-1} half-bandwidths as described before.[30b]

Crystal Structure Determinations. Single crystals of **2** and **3** were grown from a DCM/hexane solution by slow diffusion of hexanes into a saturated solution of the complexes **2** and **3** The crystallographic data for complexes **2** was collected on a Bruker Microstar generator (micro source) equipped with a Helios optics, a Kappa Nonius goniometer, and a Platinum135 detector, and crystallographic data for complex **3** was collected on a Bruker APEX II generator (X-ray sealed tube), a Kappa Nonius goniometer, and a Platinum135 detector.

Cell refinement and data reduction were done using SAINT.[31] An empirical absorption correction, based on the multiple measurements of equivalent reflections, was applied using the program SADABS.[32] The space group was confirmed by XPREP routine[33] in the program SHELXTL.[34] The structures were solved by direct-methods and refined by full-matrix least-squares and difference Fourier techniques with SHELX-97.[35] All non-hydrogen atoms were refined with anisotropic displacement parameters. Hydrogen atoms were set in calculated positions and refined as riding atoms with a common thermal parameter. Publication materials and ORTEP drawings were prepared using LinXTL and the Platon program integrated in it.

■ ASSOCIATED CONTENT

Supporting Information. The ^1H NMR spectrum of complex **2**, DFT-optimized structure coordinates, and the results of TD-DFT calculations for complexes **1** and $[\mathbf{1}]^+$. This material is available free of charge via the Internet at http://pubs.acs.org. Complete details of the X-ray analyses for complexes **2** (788986) and **3** (788985) have been deposited at The Cambridge Crystallographic Data Centre. These data can be obtained free of charge via www.ccdc.cam.ac.uk/data_request/cif, or by emailing data_request@ccdc.cam.ac.uk, or by contacting The Cambridge Crystallographic Data Centre, 12, Union Road, Cambridge CB2 1EZ, U.K.; fax: +44 1223 336033.

■ AUTHOR INFORMATION

Corresponding Author
*E-mail: zargarian.davit@umontreal.ca.

■ ACKNOWLEDGMENT

The authors gratefully acknowledge financial support received from Université de Montréal (fellowships to D.M.S.), NSERC of Canada (Research Tools and Instruments and Discovery grants to D.Z. and A.v.d.E.) and Centre for Catalysis Research and Innovation, University of Ottawa (S.I.G.).

■ REFERENCES

(1) For some of the pioneering reports on pincer complexes see: (a) Moulton, C. J.; Shaw, B. L. *J. Chem. Soc., Dalton Trans.* **1976**, 1020. (b) Crocker, C.; Errington, R. J.; McDonald, W. S.; Odell, K. J.; Shaw, B. L.; Goodfellow, R. J. *J. Chem. Soc., Chem. Commun.* **1979**, 498. (c) van Koten, G.; Timmer, K.; Noltes, J. G.; Spek, A. L. *J. Chem. Soc., Chem. Commun.* **1978**, 250. (d) Fryzuk, M. D.; MacNeil, P. A. *J. Am. Chem. Soc.* **1981**, *103*, 3592.

(2) For a selection of reviews and primary reports describing some applications of pincer complexes see: (a) Albrecht, M.; van Koten, G. *Angew. Chem., Int. Ed.* **2001**, *40*, 375. (b) van der Boom, M. E.; Milstein, D. *Chem. Rev.* **2003**, *103*, 1759. (c) Singleton, J. T. *Tetrahedron* **2003**, *59*, 1837. (d) Liang, L.-C. *Coord. Chem. Rev.* **2006**, *250*, 1152. (e) Nishiyama, H. *Chem. Soc. Rev.* **2007**, *36*, 1133. (f) Leis, W.; Mayer, H. A.; Kaska, W. C. *Coord. Chem. Rev.* **2008**, *252*, 1787. (g) Goldman, A. S.; Roy, A. H.; Huang, Z.; Ahuja, R.; Schinski, W.; Brookhart, M. *Science* **2006**, *312*, 257. (h) van der Ploeg, A. F. M. J.; van Koten, G.; Brevard, C. *Inorg. Chem.* **1982**, *21*, 2878. (i) Batema, G. D.; Lutz, M.; Spek, A. L.; van Walree, C. A.; Donegá, C. d. M.; Meijerink, A.; Havenith, R. W. A.; Pérez-Moreno, J.; Clays, K.; Büchel, M.; van Dijken, A.; Bryce, D. L.; van Klink, G. P. M.; van Koten, G. *Organometallics* **2008**, *27*, 1690. (j) Zweifel, T.; Naubron, J.-V.; Grützmacher, H. *Angew. Chem., Int. Ed.* **2009**, *48*, 559. (k) Ohff, M.; Ohff, A.; van der Boom, M. E.; Milstein, D. *J. Am. Chem. Soc.* **1997**, *119*, 11687. (l) Miyazaki, F.; Yamaguchi, K.; Shibasaki, M. *Tetrahedron Lett.* **1999**, *40*, 7379. (m) Naghipour, A.; Sabounchei, S. J.; Morales-Morales, D.; Canseco-González, D.; Jensen, C. M. *Polyhedron* **2007**, *26*, 1445. (n) Gunanathan, C.; Ben-David, Y.; Milstein, D. *Science* **2007**, *317*, 790. (o) Sebelius, S.; Olsson, V. J.; Szabo, K. J. *J. Am. Chem. Soc.* **2005**, *127*, 10478. (p) Bernskoetter, W. H.; Brookhart, M. *Organometallics* **2008**, *27*, 2036. (q) Dijkstra, H. P.; Meijer, M. D.; Patel, J.; Kreiter, R.; van Klink, G. P. M.; Lutz, M.; Spek, A. L.; Canty, A. J.; van Koten, G. *Organometallics* **2001**, *20*, 3159.

(3) Examples of bimetallic pincer complexes include the following: (a) $[\{2,6\text{-}(RSCH_2)_2C_6H_3\}Rh(H)(\mu\text{-}Cl)]_2$ (Evans, D. R.; Huang, M.; Seganish, W. M.; Chege, E. W.; Lam, Y.; Fettinger, J. C.; Williams, T. L. *Inorg. Chem.* **2002**, *41*, 2633). (b) $(CF_3PCP)Pt[\kappa1\text{-}C,\kappa3\text{-}P,C,P\text{-}2,6\text{-}(CHP(CF_3)_2)(CH_2P(CF_3)_2)\text{-}C_6H_3]PtCl$ and $[\{2,6\text{-}C_6H_3\text{-}(CH_2P(CF_3)_2\}_2Pt_2(\mu\text{-}X)]^+$ (X = H, Cl; Adams, J. J.; Arulsamy, N.; Roddick, D. M. *Organometallics* **2009**, *28*, 1148). (c) $[\{2,6\text{-bis-}(piperidylmethyl)benzene\}Pt]_2^+(\mu\text{-}L)$ (Jude, H.; Krause Bauer, J. A.; Connick, W. B. *Inorg. Chem.* **2005**, *44*, 1211, and references therein). For a few reports on dendrimers based on pincer complexes see the following reports: (d) Huck, W. T. S.; Snellink-Ruel, B.; van Veggel, F. C. J. M.; Reinhoudt, D. N. *Organometallics* **1997**, *16*, 4287. (e) Kleij, A. W.; Gossage, R. A.; Klein Gebbink, R. J. M.; Brinkmann, N.; Reijerse, E. J.; Kragl, U.; Lutz, M.; Spek, A. L.; van Koten, G. *J. Am. Chem. Soc.* **2000**, *122*, 12112. (f) Gossage, R. A.; Jastrzebski, J. T. B. H.; van Ameijde, J.; Mulders, S. J. E.; Brouwer, A. J.; Liskamp, R. M. J.; van Koten, G. *Tetrahedron. Lett.* **1999**, *40*, 1413.

(4) For a few representative studies on metal-metal interactions and electron transfer processes occurring in mixed-valent bimetallic systems see: (a) Ward, M. D. *Chem.. Soc. Rev.* **1995**, 121. (b) Gorelsky, S. I.; Xie, X.; Chen, Y.; Fee, J. A.; Solomon, E. I. *J. Am. Chem. Soc.* **2006**, *128*, 16452. (c) Hagadorn, J. R.; Zahn, T. I.; Que, L., Jr.; Tolman, W. B.

Dalton Trans. **2003**, 1790. (d) Ernst, S.; Kasack, V.; Kaim, W. *Inorg. Chem.* **1988**, *27*, 1146. (e) Gamelin, D. R.; Randall, D. W.; Hay, M. T.; Houser, R. P.; Mulder, T. C.; Canters, G. W.; de Vries, S.; Tolman, W. B.; Lu, Y.; Solomon, E. I. *J. Am. Chem. Soc.* **1998**, *120*, 5246. (f) Atwood, C. G.; Geiger, W. E. *J. Am. Chem. Soc.* **2000**, *122*, 5477. (g) Lu, C. C.; Bill, E.; Weyhermüller, T.; Bothe, E.; Wieghardt, K. *J. Am. Chem. Soc.* **2008**, *130*, 3181. (h) Xie, X.; Gorelsky, S. I.; Sarangi, R.; Garner, D. K.; Hwang, H. J.; Hodgson, K. O.; Hedman, B.; Lu, Y.; Solomon, E. I. *J. Am. Chem. Soc.* **2008**, *130*, 5194.

(5) (a) Groux, L. F.; Bélanger-Gariépy, F.; Zargarian, D. *Can. J. Chem.* **2005**, *83*, 634. (b) Castonguay, A.; Sui-Seng, C.; Zargarian, D.; Beauchamp, A. L. *Organometallics* **2006**, *25*, 602. (c) Sui-Seng, C.; Castonguay, A.; Chen, Y.; Gareau, D.; Groux, L. F.; Zargarian, D. *Top. Catal.* **2006**, *37*, 81. (d) Castonguay, A.; Beauchamp, A. L.; Zargarian, D. *Acta Crystallogr.* **2007**, *E63*, m196. (e) Pandarus, V.; Zargarian, D. *Chem. Commun.* **2007**, 978. (f) Pandarus, V.; Zargarian, D. *Organometallics* **2007**, *26*, 4321. (g) Castonguay, A.; Beauchamp, A. L.; Zargarian, D. *Organometallics* **2008**, *27*, 5723. (h) Castonguay, A.; Spasyuk, D. M.; Madern, N.; Beauchamp, A. L.; Zargarian, D. *Organometallics* **2009**, *28*, 2134. (i) Spasyuk, D. M.; Zargarian, D.; van der Est, A. *Organometallics* **2009**, *28*, 6531. (j) Spasyuk, D. M.; Zargarian, D. *Inorg. Chem.* **2010**, *49*, 6203.

(6) Designation of the pincer ligand in **1** as LXX-type is warranted in the sense that it is, in its closed shell form, a dianionic ligand (or a diradical if the covalent bonding model is applied). On the other hand, it is instructive to note that the Ni-N distances between different halves of the dimer are shorter than those in each half (see X-ray structure of **1** in ref 5j), and that this trend is confirmed by the calculated Ni-N bond orders (vide supra). These observations imply greater covalent character in the Ni-N bonds that are *trans* to the aryl moiety and suggest, in turn, that the dimeric complex **1** can be viewed as two (LXL′)Ni halves bridged through primarily Ni-amide type interactions involving the L′ moieties.

(7) (a) Atkins, A. J.; Blake, A. J.; Schröder, M. *Chem. Commun.* **1993**, 1662. (b) Branscombe, N. D. J.; Atkins, A. J.; Marin-Becerra, A.; McInnes, E. J. L.; Mabbs, F. E.; McMaster, J.; Schröder, M. *Chem. Commun.* **2003**, 1098.

(8) van Gastel, M.; Shaw, J. L.; Blake, A. J.; Flores, M.; Schröder, M.; McMaster, J.; Lubitz, W. *Inorg. Chem.* **2008**, *47*, 11688.

(9) (a) op den Brouw, P. M.; van der Linden, J. G. M. *Inorg. Nucl. Chem. Lett.* **1977**, *13*, 149. (b) Huang, D.; Deng, L.; Sun, J.; Holm, R. *Inorg. Chem.* **2009**, *48*, 6159. This complex features a dianionic XLX-type SNS ligand; no structural studies have been conducted on this species because of its limited solubility.

(10) Adhikari, D.; Mossin, S.; Basuli, F.; Dible, B. R.; Chipara, M.; Fan, H.; Huffman, J. C.; Meyer, K.; Mindiola, D. J. *Inorg. Chem.* **2008**, *47*, 10479. It should be added that, strictly speaking, this compound is not a pincer-type species because the two neutral donor moieties of the PNP ligand are bound to different nickel centers, while it is the central amido moiety that serves as bridge. Thus, the PNP ligand spans across the two nickel centers and does not impose a meridional coordination environment on them.

(11) It should be noted that a wider-than-anticipated difference in the potentials for anodic and cathodic waves (on the order of ca. 0.080−0.120 V) is a common feature of the cyclic voltammograms obtained for DCM solutions of all nickel pincer complexes examined by us. That one-electron processes are at work in these systems is supported by the results obtained from square-wave-voltammetry experiments and by the fact that, under the experimental conditions employed during our studies, ferrocene also produces similar peak-to-peak separations.

(12) All redox potentials noted in this report are referenced to the $Cp_2Fe/[Cp_2Fe]^+$ couple.

(13) Analogous amide-to-imine transformations in pincer-type complexes have been reported by Milstein's group; see ref.2n and Zhang, J.; Leitus, G.; Ben-David, Y.; Milstein, D. *J. Am. Chem. Soc.* **2005**, *127*, 10840–10841.

(14) (a) Grove, D. M.; van Koten, G.; Mul, P.; Zoet, R.; van der Linden, J. G. M.; Legters, J.; Schmitz, J. E. J.; Murrall, N. W.; Welch, A. J. *Inorg. Chem.* **1988**, *27*, 2466–2473. (b) Grove, D. M.; van Koten, G.; Mul, W. P.; van der Zeijden, A. A. H.; Terheijden, J.; Zoutberg, M. C.; Stam, C. H. *Organometallics* **1986**, *5*, 322–326. (c) Grove, D. M.; van Koten, G.; Zoet, R.; Murrall, N. W.; Welch, A. J. *J. Am. Chem. Soc.* **1983**, *105*, 1379–1380. (d) Kozhanov, K. A.; Bubnov, M. P.; Cherkasov, V. K.; Fukin, G. K.; Vavilina, N. N.; Efremova, L. Y.; Abakumov, G. A. *J. Magn. Reson.* **2009**, *197*, 36–39.

(15) Kivelson, D.; Neiman, R. *J. Chem. Phys.* **1961**, *35*, 156–161.

(16) (a) Becke, A. D. *J. Chem. Phys.* **1993**, *98*, 5648. (b) Lee, C.; Yang, W.; Parr, R. G. *Phys. Rev. B* **1988**, *37*, 785.

(17) Schafer, A.; Huber, C.; Ahlrichs, R. *J. Chem. Phys.* **1994**, *100*, 5829–5835.

(18) (a) Casida, M. E. . In *Recent Advances in Density Functional Methods*; Chong, D. P., Ed.; World Scientific: Singapore, 1995; p 155. (b) Stratmann, R. E.; Scuseria, G. E.; Frisch, M. J. *J. Chem. Phys.* **1998**, *109*, 8218.

(19) For an interpretation of computed bond orders, please see: Gorelsky, S. I.; Basumallick, L.; Vura-Weis, J.; Sarangi, R.; Hedman, B.; Hodgson, K. O.; Fujisawa, K.; Solomon, E. I. *Inorg. Chem.* **2005**, *44*, 4947–4960.

(20) Reed, A. E.; Weinstock, R. B.; Weinhold, F. *J. Chem. Phys.* **1985**, *83*, 735.

(21) Mayer, I. *Chem. Phys. Lett.* **1983**, *97*, 270–274.

(22) It should be noted that the calculated sum of spin present on the four atoms in Ni_2N_2 core in $[\mathbf{1}]^{+\cdot}$ is 1.06, but the sum of all atomic spin densities in $[\mathbf{1}]^{+\cdot}$ is still 1.0. This is because some ligand atoms possess negative spin densities due to spin-polarization effects.

(23) Robin, M. B.; Day, P. *Adv. Inorg. Chem. Radiochem.* **1967**, *10*, 247.

(24) We have also considered an alternative reaction pathway involving initial oxidation at the ligand to generate an intermediate featuring a Ni-coordinated aminyl radical. Such a species could undergo H-abstraction by the in situ generated succinimide radical to give **3**, or abstract H from the reaction medium to generate **4**. However, this scenario would require more than 2 equiv of oxidant for the formation of the ultimate product, **2**.

(25) Buttner, T.; Geier, J.; Frison, G.; Harmer, J.; Calle, C.; Schweiger, A.; Schonberg, H.; Grützmacher, H. *Science* **2005**, *307*, 235.

(26) Adhikari, D.; Mossin, S.; Basuli, F.; Huffman, J. C.; Szilagyi, R. K.; Meyer, K.; Mindiola, D. J. *J. Am. Chem. Soc.* **2008**, *130*, 3676.

(27) For a recent discussion on the characterization and potential applications of metal complexes bearing aminyl radicals see: Hicks, R. G. *Angew. Chem., Int. Ed.* **2008**, *47*, 7393.

(28) Frisch, M. J.; Trucks, G. W.; Schlegel, H. B.; Scuseria, G. E.; Robb, M. A.; Cheeseman, J. R.; Scalmani, G.; Barone, V.; Mennucci, B.; Petersson, G. A.; Nakatsuji, H.; Caricato, M.; Li, X.; Hratchian, H. P.; Izmaylov, A. F.; Bloino, J.; Zheng, G.; Sonnenberg, J. L.; Hada, M.; Ehara, M.; Toyota, K.; Fukuda, R.; Hasegawa, J.; Ishida, M.; Nakajima, T.; Honda, Y.; Kitao, O.; Nakai, H.; Vreven, T.; Montgomery, J. A.; , Jr., Peralta, J. E.; Ogliaro, F.; Bearpark, M.; Heyd, J. J.; Brothers, E.; Kudin, K. N.; Staroverov, V. N.; Kobayashi, R.; Normand, J.; Raghavachari, K.; Rendell, A.; Burant, J. C.; Iyengar, S. S.; Tomasi, J.; Cossi, M.; Rega, N.; Millam, J. M.; Klene, M.; Knox, J. E.; Cross, J. B.; Bakken, V.; Adamo, C.; Jaramillo, J.; Gomperts, R.; Stratmann, R. E.; Yazyev, O.; Austin, A. J.; Cammi, R.; Pomelli, C.; Ochterski, J. W.; Martin, R. L.; Morokuma, K.; Zakrzewski, V. G.; Voth, G. A.; Salvador, P.; Dannenberg, J. J.; Dapprich, S.; Daniels, A. D.; Farkas, O.; Foresman, J. B.; Ortiz, J. V.; Cioslowski, J.; , Fox, D. J. *Gaussian 09*, Revision A.02; Gaussian, Inc.: Wallingford, CT, 2009.

(29) Mayer, I. *Int. J. Quantum Chem.* **1986**, *29*, 73.

(30) (a) Gorelsky, S. I. *AOMix, Program for Molecular Orbital Analysis*, Version 6.46; University of Ottawa: Ottawa, Canada, 2010. (b) Gorelsky, S. I.; Lever, A. B. P. *J. Organomet. Chem.* **2001**, *635*, 187.

(31) *SAINT, Integration Software for Single Crystal Data*, Release 6.06; Bruker AXS Inc.: Madison, WI, 1999.

(32) Sheldrick, G. M. *SADABS, Bruker Area Detector Absorption Corrections*; Bruker AXS Inc.: Madison, WI, 1999.

(33) *XPREP, X-ray data Preparation and Reciprocal space Exploration Program*, Release 5.10; Bruker AXS Inc.: Madison, WI, 1997.

(34) *SHELXTL, The Complete Software Package for Single Crystal Structure Determination*, Release 5.10; Bruker AXS Inc.: Madison, WI, 1997.

(35) (a) Sheldrick, G. M.*SHELXS97, Program for the Solution of Crystal Structures*; University of Göttingen: Göttingen, Germany, 1997. (b) Sheldrick, G. M. *SHELXL97, Program for the Refinement of Crystal Structures*; University of Göttingen: Göttingen, Germany, 1997.